Detectability of finite-temperature effects from neutron star mergers with next-generation gravitational wave detectors

Carolyn A. Raithel[1,2] and Vasileios Paschalidis[3,4]

[1]*School of Natural Sciences, Institute for Advanced Study, 1 Einstein Drive, Princeton, New Jersey 08540, USA*
[2]*Princeton Gravity Initiative, Jadwin Hall, Princeton University, Princeton, New Jersey 08540, USA*
[3]*Department of Astronomy and Steward Observatory, University of Arizona, 933 North Cherry Avenue, Tucson, Arizona 85721, USA*
[4]*Department of Physics, University of Arizona, 1118 E. Fourth Street, Arizona 85721, USA*

(Received 21 December 2023; accepted 28 June 2024; published 2 August 2024)

Observations of the high-frequency gravitational waves (GWs) emitted by the hot and massive remnant of a binary neutron star merger will provide new probes of the dense-matter equation of state (EOS). We show that current uncertainties in the thermal physics can cause the emergent GW spectum to differ by a degree comparable to changing the cold EOS by $\pm \sim 120$ m in the characteristic radius of a neutron star. Unless a very close binary neutron star merger takes place, these effects are unlikely to be measurable with current GW detectors. However, with proposed next-generation detectors such as Cosmic Explorer or Einstein Telescope, the effects can be distinguished for events at distances of up to ∼80–200 Mpc, if the cold EOS is sufficiently well constrained.

DOI: 10.1103/PhysRevD.110.043002

I. INTRODUCTION

Following a binary neutron star merger, if the masses of the initial neutron stars are within a certain range, the remnant can survive as a metastable, hypermassive or supramassive neutron star which will emit high-frequency gravitational waves that are sensitive to the details of the underlying equation of state (EOS) [1–5]. Depending on the EOS, these postmerger gravitational waves (GWs) peak at frequencies of 2–4 kHz, with softer EOSs (which predict more compact neutron stars) leading to higher peak frequencies, and stiffer EOSs (which predict larger-radius neutron stars) generally leading to lower peak frequencies [6–9]. See also [10,11].

Because the postmerger GWs peak at frequencies well above the ∼100 Hz regime where the current generation of detectors are most sensitive, measuring these signals with the existing network of GW detectors will require either a very nearby source ($\lesssim$30 Mpc [12]) and/or the development of new data analysis techniques, e.g., for mode stacking of individual events [13]. On the other hand, with the construction of next-generation (XG) GW detectors, such as the proposed Cosmic Explorer (CE) [14], Einstein Telescope (ET) [15], or NEMO [16] detectors, these signals are expected to be detectable within $\lesssim$1 year of operations [13,17,18].

One key difference between the EOS constraints that have been placed using inspiral GWs [e.g., [19–24]] and what will be probed with the postmerger GWs in the near future, is that whereas the inspiraling neutron stars are thermodynamically cold, the postmerger remnant is significantly shock heated, with thermal pressures that can be a significant fraction ($\gtrsim$10% at supranuclear densities) of the cold pressure (e.g., [25–33]). As a result, the emergent GW spectrum is sensitive not only to uncertainties in our knowledge of the cold physics, but also to our uncertain knowledge of the finite-temperature EOS [26,33–37].

Finite-temperature effects have been shown to shift the spectrum of postmerger GWs by up to ∼60–200 Hz for realistic thermal prescriptions [33,35–37], with larger shifts of the peak frequency found when the cold EOS is relatively soft (i.e., predicts smaller radius neutron stars, leading to more violent collisions and stronger shock heating) [33].

In this work, we expand on our recent study of finite-temperature effects in neutron star merger simulations [33], and we quantify the distinguishability of different prescriptions of the thermal physics in the postmerger GWs. We compare the impact of these thermal effects to a set of new simulations that explore the impact of making small (few percentage) variations to the cold EOS. We find that, for a baseline EOS model that predicts a characteristic neutron star radius of $R_{1.4} \approx 11$ km, the uncertainty in the thermal physics leads to a comparable change in the postmerger GWs as changing the cold EOS by ± 120 m in $R_{1.4}$ or by ± 15 in the corresponding tidal deformabilty. This level of uncertainty in the cold EOS is expected to be pinned down from inspiral GWs within one year of observations for an XG detector such as CE [38–40]. Thus,

by combining EOS constraints from the (cold) inspiral with a detection of the postmerger GWs from the hot neutron star remnant, these results suggest that it will become possible to constrain the *finite-temperature* part of the EOS in the XG era, at least for the thermal models considered here and assuming other second-order effects (e.g., out-of-equilibrium effects [41–43]) are sufficiently well understood.

We quantify the distinguishability of thermal effects in the postmerger GWs with current and upcoming GW detectors. We find that thermal effects are easier to distinguish for a stiffer EOS than for a softer EOS, even though there is significantly less heating for the stiff EOS and the shifts to the dominant peak frequencies are accordingly smaller.

We conservatively estimate that the thermal effects studied here could be resolved at distances of up to ∼200 Mpc for a stiff ($R_{1.4} \approx 14$ km) EOS and up to ∼80 Mpc for a soft ($R_{1.4} \approx 11$ km) EOS, with the sensitivity of a 20 km Cosmic Explorer detector that has been tuned to optimize postmerger sensitivity [44], if the cold EOS is well known (see also [36]). With the design sensitivity of aLIGO, a merger would have to be within $\lesssim$10 Mpc to measure these thermal effects. We compare these prospects with the proposed sensitivity of ET and with a 40 km configuration of CE and determine that the 20 km "postmerger tuned" configuration of CE leads to the best prospects for measuring finite-temperature effects directly from the postmerger GWs. We note that a full detectability analysis—including a framework to measure the statistical significance of the inferred thermal parameters—would require a parameter estimation study, which is beyond the scope of the present work. Nevertheless, our results indicate that the prospects are optimistic for distinguishing these thermal prescriptions from neutron star mergers at realistic distances, with the projections for all three of the proposed next-generation detectors.

II. NUMERICAL METHODS

In this work, we explore the observability of finite-temperature effects in the postmerger GWs from a binary neutron star merger. To that end, we analyze the GW signals from a set of simulations that were designed to systematically disentangle the relative roles of the uncertainties in the zero-temperature and finite-temperature parts of the EOS. Some of these simulations were previously presented in [33]. We briefly review the key details of the setup here, but for further details see [33] (hereafter, Paper I).

A. Construction of finite-temperature equations of state

In both the simulations of Paper I and the new simulations performed in this work, we use the phenomenological framework of [45] for calculating the EOS. In this framework, the total pressure is decomposed into a cold and thermal component, according to

$$P_{\rm total}(n, T, Y_e) = P_{\rm cold}(n, T = 0, Y_e) + P_{\rm th}(n, T, Y_e), \quad (1)$$

where n is the baryon number density, T is the temperature, and Y_e is the electron fraction, which we fix to the initial β-equilibrium configuration. For the cold EOSs, we adopt two different generalized-piecewise polytropic EOSs [33,46], which predict characteristic neutron star radii of $R_{1.4} \approx$ 11 km and 14 km.

We additionally construct modified versions of the softer ($R_{1.4} \approx 11$ km) model, which vary from the baseline model by $\Delta R_{1.4} = -120, -54$, and $+116$ m (or equivalently, by up to $\pm 5\%$ in the cold pressure at supranuclear densities; see Appendix A for details). This range of cold EOSs is motivated by projections that Cosmic Explorer will measure the neutron star radius to within 50–200 m within one year of inspiral observations [39,40]. Thus, this set of cold EOSs brackets the degree of variation that is expected to be constrained in the XG era.

To each cold EOS, we attach one of four prescriptions for the thermal pressure, calculated using the "M^* framework" of [45], which captures the leading-order effects of degeneracy in the thermal prescription by parametrizing the particle effective mass, M^*. The framework has been shown to accurately recreate full EOS tables both analytically [45] and in the context of merger simulations [47]. The four thermal prescriptions used here correspond to four choices of M^* parameters, including density parameters $n_0 \in (0.08, 0.22)$ fm^{-3}, which describe the density at which the effective mass starts to decay from its vacuum rest mass, and power-law parameters $\alpha \in (0.6, 1.3)$, which characterize the rate at which M^* decreases with density. This range of parameters was found previously to bracket the range of best-fit values for realistic calculations of the effective mass function for commonly-used finite-temperature EOSs [45]. We refer to these parameter sets as Thermal Cases I–IV in the following.

We attach each of the four thermal prescriptions to the $R_{1.4} \approx 11$ km and $R_{1.4} \approx 14$ km cold EOS models (for a total of eight finite-temperature EOSs), to explore the sensitivity of the merger to the choice of thermal treatment. To the set of modified $R_{1.4} \approx 11$ km EOSs, we attach a single thermal treatment (Case I), to explore the sensitivity of the merger to small variations in the cold EOS with a fixed thermal treatment. We summarize the EOSs thus constructed in Tables I and II.

B. Initial conditions and numerical setup

For the new simulations performed in this work, the numerical set-up is identical to that used for the $R_{1.4} \approx$ 11 km evolutions in Paper I [33]. In summary, for each EOS, we perform a simulation of an equal-mass $(1.3 + 1.3 M_\odot)$ binary neutron star merger in full general relativity using the code of [48–51], as it has been recently extended in [32,52].

TABLE I. Summary of the simulations varying the thermal treatment, for two different cold EOSs. From left to right, the columns indicate the cold EOS, the thermal prescription, the M^* parameters (n_0 and α), the density-weighted average of the thermal pressure relative to the cold pressure, and the peak GW frequency. The averages are computed including all matter with densities $\rho \geq \rho_{\rm sat}$.

Cold EOS	Thermal case	M^* parameters	$\langle P_{\rm th}/P_{\rm cold}\rangle$	f_2 [kHz]
$R_{1.4} \approx 11$ km	I	(0.08 fm^{-3}, 0.6)	0.33	3.35
	II	(0.08 fm^{-3}, 1.3)	0.27	3.50
	III	(0.22 fm^{-3}, 0.6)	0.34	3.33
	IV	(0.22 fm^{-3}, 1.3)	0.40	3.48
$R_{1.4} \approx 14$ km	I	(0.08 fm^{-3}, 0.6)	0.12	2.62
	II	(0.08 fm^{-3}, 1.3)	0.12	2.57
	III	(0.22 fm^{-3}, 0.6)	0.10	2.63
	IV	(0.22 fm^{-3}, 1.3)	0.14	2.58

TABLE II. Summary of simulations varying the cold ($R_{1.4} \approx 11$ km) EOS. The first two columns indicate the deviations, relative to the baseline model, for the radius and tidal deformability of a $1.4M_\odot$ neutron star. All simulations use thermal prescription I. The baseline case is identical to the $R_{1.4} \approx 11$ km entry from Table I, with M^* parameters (0.08 fm^{-3}, 0.6).

Cold EOS	$\Lambda_{1.4}$	$\langle P_{\rm th}/P_{\rm cold}\rangle$	f_2 [kHz]
$\Delta R_{1.4} = -120$ m	$\Delta\Lambda_{1.4} = -16$	0.36	3.18
$\Delta R_{1.4} = -54$ m	$\Delta\Lambda_{1.4} = -7$	0.28	3.35
Baseline [$R_{1.4} = 11.1$ km]	$\Lambda_{1.4} = 230$	0.33	3.35
$\Delta R_{1.4} = +116$ m	$\Delta\Lambda_{1.4} = +14$	0.28	3.46

The initial neutron stars are constructed using LORENE2 [53], and are cold, irrotational, unmagnetized, and placed at an initial coordinate separation of 40 km.

Our simulations use nine spatial refinement levels, which are separated by a 2:1 refinement ratio. The grid spacing on the innermost refinement level corresponds to $\Delta x = 140$ m, such that the coordinate diameter of the initial neutron stars is covered by ∼125 grid points (where the initial coordinate radius of this model is 8.76 km along the x direction). For the $R_{1.4} \approx 14$ km EOSs, the grid spacing on the innermost refinement level is $\Delta x = 195$ m, for the same effective grid coverage across the initial neutron stars (with initial coordinate radii of 12.10 km).

III. RESULTS

For all cases, we evolve the neutron stars through the final 3–4.5 orbits of the inspiral, through the merger, and for the first 12 ms postmerger (for the $R_{1.4} \approx 11$ km models) and the first 20 ms postmerger (for the $R_{1.4} \approx 14$ km models), in order to extract the properties of the postmerger remnant and the emergent GW signal. We note that the unequal lengths of the simulations are necessary to capture the salient features of the postmerger GW emission, which are more temporally-extended for the stiffer cold EOS. Spectrograms of the GW signals for these models, and additional discussion of their temporal differences, can be found in Appendix B.

In this work, we focus primarily on the spectra of postmerger GWs, as the key observable feature from such events. Nevertheless, to give a sense of the different degrees of heating experienced in each evolution, Tables I and II also report the average thermal pressure relative to the cold pressure, $\langle P_{\rm th}/P_{\rm cold}\rangle$, within the late-time remnants, for each EOS. These averages are density weighted and include all matter with densities $\geq \rho_{\rm sat}$ (where $\rho_{\rm sat} = 2.7 \times 10^{14}$ g/cm^3 is the nuclear saturation density), in order to highlight the heating in the dense-matter core. The summary features from the sequence of EOSs that vary in their thermal treatment, while holding the cold EOS fixed, are shown in Table I (for further analysis of these evolutions, see Paper I). The summary features from the new simulations, for the systematic variations to the cold $R_{1.4} \approx 11$ km EOS, are summarized in Table II.

A. Postmerger GW spectra

We extract the GW signal from each of our simulations using the Newman-Penrose formalism. The resulting spectra of GWs are characterized by three main spectral peaks, as is typical of such simulations [e.g., [1,2,8,54–56]]. However, the spectra also exhibit small-scale noise on top of these spectral peaks, which can originate either from numerical error or from turbulent motions in the remnant following the merger. This high-frequency noise can artificially inflate estimates of the differentiability between

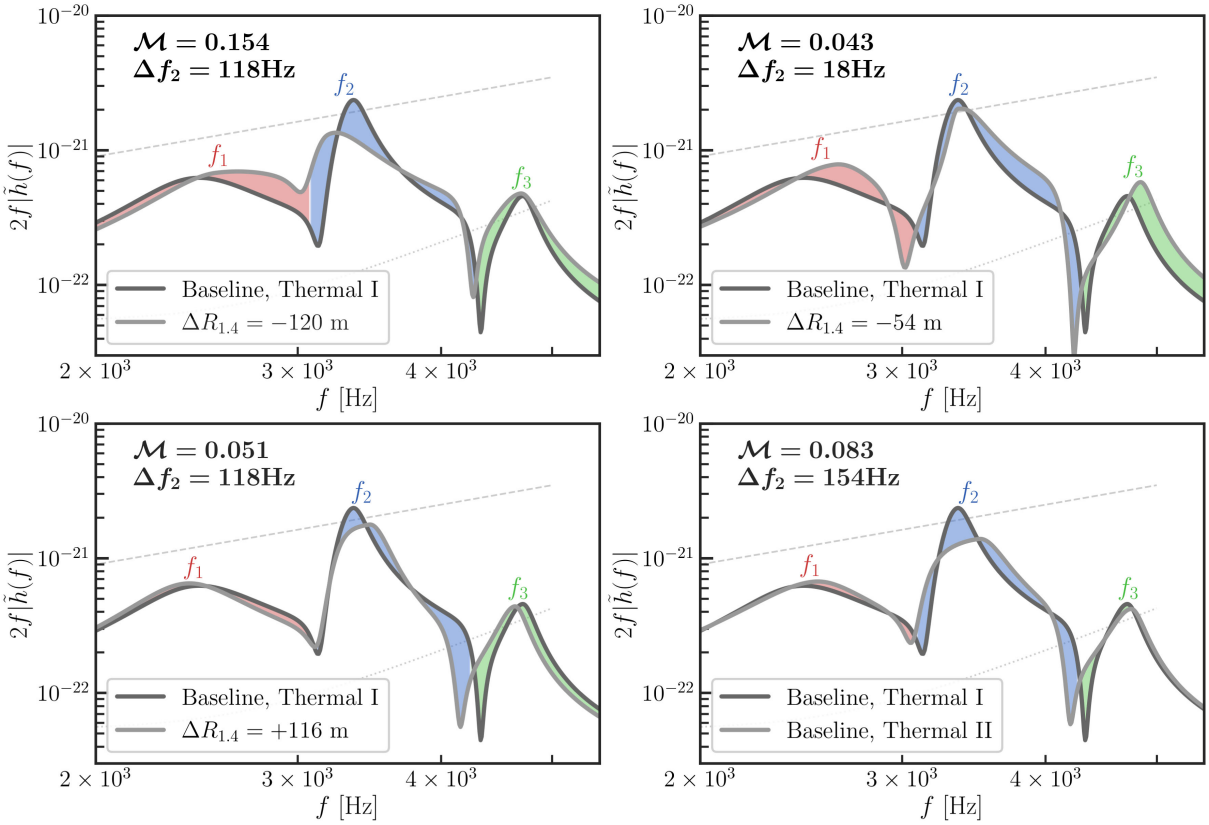

FIG. 1. Postmerger GW spectra for a subset of the $R_{1.4} \approx 11$ km evolutions. We show here the best-fit templates for each simulation, based on a model comprising three skew-Lorentzian peaks (see Appendix C for details). The dashed and dotted lines indicate the sensitivity of aLIGO at design sensitivity [57] and CE in the 20 km configuration tuned for postmerger sensitivity [44], respectively. Spectra include the dominant $\ell = m = 2$ mode and assume a face-on orientation for a source directly overhead and at a distance of 40 Mpc. The top row and bottom left panels show the impact of varying the cold EOS by -120, -54, and $+116$ m in radius (or, equivalently, scaling the supranuclear pressure by up to $\pm 5\%$). The lower right panel shows the impact of varying the α parameter of the M^* thermal prescription. The color coding is included to help visually distinguish the three spectral peaks (labeled f_1, f_2, and f_3) and to highlight the mismatch between each pair of spectra.

the spectra. In order to minimize the impact of this noise on our analysis, we fit the (frequency-domain) spectra with smooth templates that are constructed to capture the dominant spectral features of the simulations. Our templates thus comprise three Lorentzian profiles, which allow for nonzero skew in each peak. We perform a least-squares minimization to fit the parameters of these template models to the spectra (for details, see Appendix C). We find that the best-fit templates are able to reliably reproduce the raw spectra, while reducing the dependence of our subsequent analysis on the small-scale noise. In particular, for estimating the distinguishability of the spectra, we find that using the templates always provides a more *conservative* estimate than would be estimated from the raw spectra. For additional discussion, see Appendix C.

We show the resulting, best-fit templates to the postmerger GWs for several pairs of EOSs in Figs. 1 and 2.

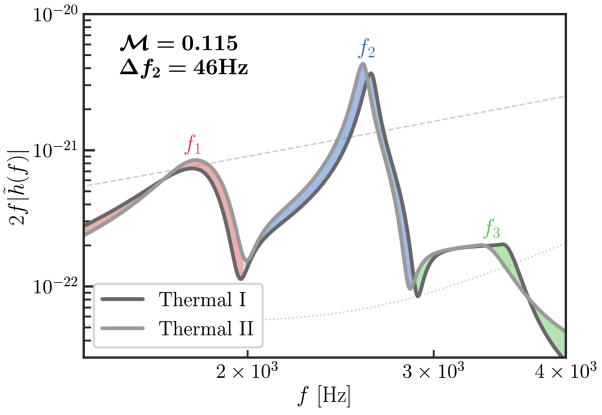

FIG. 2. Same as the bottom right panel of Fig. 1, but for the scenario in which the thermal treatment is varied (from Case I to Case II) and the cold EOS is held fixed to the $R_{1.4} \approx 14$ km model.

In the top row and bottom left panels of Fig. 1, we show the spectra from the simulations performed for the new cold EOSs, and include the baseline $R_{1.4} \approx 11$ km model with the same thermal treatment (Case I) for reference. In the bottom right panel of Fig. 1, we compare two choices for the thermal treatments (Case I and II), for which the cold EOS is held fixed to the $R_{1.4} \approx 11$ km model. Figure 2 shows the same comparison of the Case I and II thermal treatments, but for the evolutions in which the cold EOS is fixed to the $R_{1.4} \approx 14$ km model.

These figures label the three dominant peaks (f_1, f_2, and f_3) and color code these spectral peaks in red, blue, and green, for visual clarity. In addition, in the top corner of each subplot, Figs. 1 and 2 also report the differences in peak frequency, f_2, between each pair of EOSs shown, as well as the relative mismatch of the two spectra. We calculate the mismatch as

$$\mathcal{M} = 1 - \frac{\langle h_1|h_2\rangle}{\sqrt{\langle h_1|h_1\rangle\langle h_2|h_2\rangle}}, \tag{2}$$

where $\langle h_i|h_j\rangle$ indicates the noise-weighted inner product between the two waveforms, computed in the frequency domain according to

$$\langle h_i|h_j\rangle = 4\Re \int_{f_{\rm min}}^{f_{\rm max}} \frac{\tilde{h}_i(f)\tilde{h}_j^*(f)}{S_n(f)} df. \tag{3}$$

In this equation, $S_n(f)$ is the power spectral density of the detector noise, which we take (unless otherwise noted) to be that of CE in the 20 km configuration tuned for postmerger sensitivity [44]. The asterisk in Eq. (3) indicates the complex conjugate of the strain and the integrals are computed over a frequency range $f_{\rm min} = 2$ kHz (1.4 kHz) to $f_{\rm max} = 5.5$ kHz (4 kHz), for the $R_{1.4} \approx 11$ km ($R_{1.4} \approx 14$ km) EOSs. This choice of frequencies approximately brackets the postmerger signal, which we define as beginning just below the instantaneous GW frequency at the merger and ending where the spectral amplitude decreases by $\sim 100\times$ from the peak. We report the mismatches after minimization with respect to phase and time shifts [58,59] and using the best-fit spectral templates, which we find leads to mismatches that are typically smaller than (~ 0.2–$0.8\times$) the mismatches calculated from the raw spectra. As such, the templates provide a conservative, lower-limit estimate of distinguishability.

For reference, we include in Appendix C the best-fit templates and corresponding mismatches for two simulations performed at two different resolutions (the higher of which matches the effective resolutions of the $R_{1.4} \approx 11$ km and $R_{1.4} \approx 14$ km evolutions), for an EOS with an intermediate stiffness and choice of M^* parameters. For the two resolutions studied, we find only a small difference in the peak frequencies of 26 Hz and a mismatch between the best-fit templates of 0.037, which provides an approximate reference baseline for the following discussion.

In comparing pairs of models that differ by small degrees in the cold EOS, we find differences of up to 118 Hz in the peak frequency, with the largest difference for the cases of either $\Delta R_{1.4} = -120$ m or $+116$ m, compared to the baseline model. Of the models considered in Fig. 1, the case of $\Delta R_{1.4} = -120$ m also has the largest mismatch with respect to the baseline model, with significant misalignments visible around not only the dominant (second) peak, but around the first peak as well. For the case of $\Delta R_{1.4} = -54$ m, we find negligible differences in the peak frequency, but that there is still a significant mismatch, due to the differences around the first peak. At the other extreme, for the $\Delta R_{1.4} = +116$ m case, we find that the first peaks are very closely aligned, and that the second peak dominates the mismatch.

The magnitude of these spectral shifts from small changes to the cold EOS are comparable to—and in some cases smaller than—the impact of changing the thermal treatment. The lower right panel of Fig. 1 shows one representative comparison of thermal effects, for the $R_{1.4} \approx 11$ km cold EOS with two different choices of the M^* parameter α, which was found in Paper I to govern the location of the peak frequency of the postmerger spectra. The difference in f_2 for these two thermal treatments is 154 Hz, slightly larger than changing the cold EOS by $\Delta R_{1.4} = \pm 120$ m. We note that this effect is typical of the changes to f_2 found for varying values of the thermal parameter, α. We show additional examples between the other thermal cases in Appendix C. Moreover, we find that the different thermal prescriptions (in the bottom right of Fig. 1, as well as for those shown in Appendix C) lead to a comparable (and in some cases) larger mismatch than changing the cold EOS by -54 m to $+116$ m. Notably, the misalignment is visibly dominated by the dominant (second) peak when the thermal prescription is changed.

For the case of a stiffer cold EOS ($R_{1.4} \approx 14$ km), the differences in peak frequency are generally smaller ($\lesssim 60$ Hz), though there are still significant mismatches ($\mathcal{M} \sim 0.1$–0.26), depending on the choice of the thermal parameter, α (see Fig. 2 and Appendix C). This further highlights that small differences in f_2 can correspond to spectra with large mismatches, and that the thermal effects can have a significant effect on the postmerger spectra.

B. Frequency dependence of the spectral mismatches

In order to further understand the sensitivity of the spectra to changes in the underlying EOS, the top panels of Figs. 3 and 4 show the mismatches calculated for the first two peaks individually, which are the most observationally relevant features, given that the third peaks occur at higher frequencies which are unlikely to be resolved even with XG detectors. We define the mismatch of Peak 1 ($\mathcal{M}_1$; shown visually as the red shaded regions in Figs. 1 and 2) via

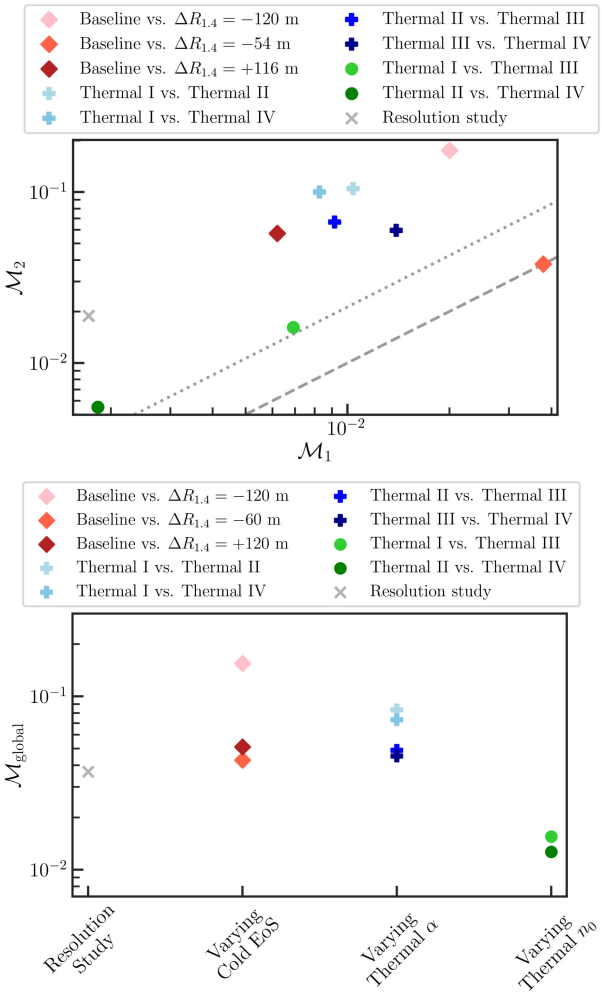

FIG. 3. Top: mismatch of the first two peaks (corresponding to the red and blue shaded regions from Fig. 1) for various pairs of $R_{1.4} \approx 11$ km EOSs. Bottom: global mismatches (calculated from 2 to 5.5 kHz) for the same models. Comparisons for which the cold EOS has been varied are shown in red diamonds. Comparisons for which the cold EOS is held fixed (to $R_{1.4} \approx 11$ km) and the thermal treatment have been varied are shown in blue crosses (for different choices of the M^* parameter α) and green circles (for different choices of the M^* parameter n_0). The gray x indicates the mismatches for two different resolutions and an EOS of intermediate stiffness ($R_{1.4} \approx 12$ km) and choice of M^* parameters. Finally, the dashed gray line in the top figure indicates the line of equal mismatches while the dotted gray line indicates where the horizon distances [Eq. (4)] would be equal.

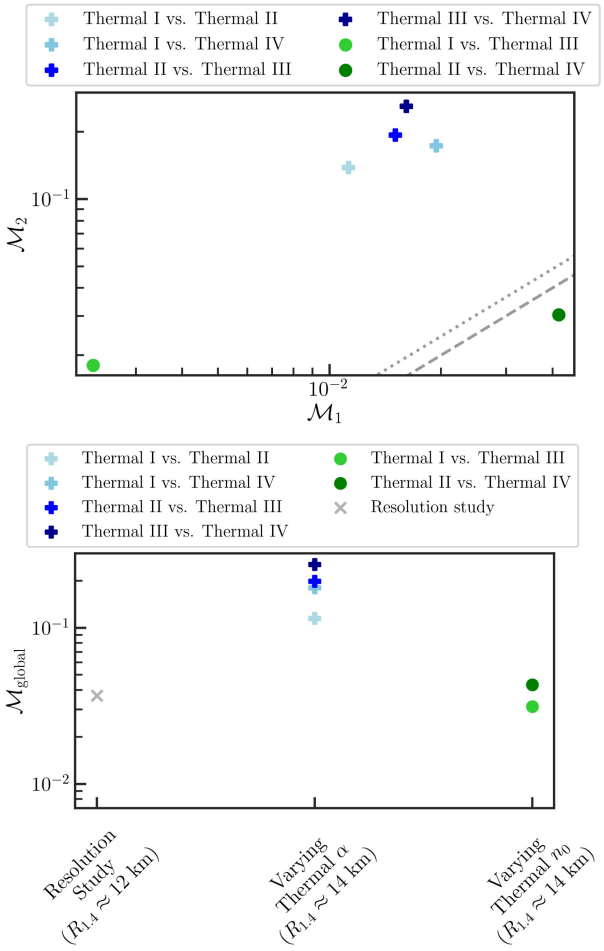

FIG. 4. Same as Fig. 3, but for the set of $R_{1.4} \approx 14$ km EOSs that vary in their thermal component. The resolution study (for an $R_{1.4} \approx 12$ km EOS) is repeated, for reference.

Eqs. (2) and (3), with frequency bounds between $f_{\rm min}$ and the average of the first minima of the two spectra being considered. The mismatch of Peak 2 ($\mathcal{M}_2$; corresponding to the blue shaded regions in Figs. 1 and 2) is likewise calculated between the average first minima and the average second minima of the two spectra being compared.

As was seen visually in Fig. 1 for the case of the $R_{1.4} \approx 11$ km models, Fig. 3 further demonstrates that the $\Delta R_{1.4} = -120$ and -54 m cases are characterized by relatively large mismatches in their first peaks. All of the cases for which the thermal treatment is varied have smaller mismatches in their first peaks. In other words, varying the cold EOS toward smaller radii has a significant effect on not only the dominant spectral peak, but also the lower-frequency first peak. In contrast, varying the thermal prescriptions seems to primarily affect the second (dominant) spectral peak. This has significant implications for the detectability of these spectral differences, as we discuss further below.

The bottom panel of Fig. 3 shows the global mismatches for the same models, calculated across the entire postmerger frequency range from $f_{\rm min} = 2$ kHz to $f_{\rm max} = 5.5$ kHz. We see here that changing the α parameter of the thermal prescription (which governs the power-law decay of the effective mass with density) leads to global mismatches that are comparable to changing the cold EOS by -54 to $+116$ m, for all of the $R_{1.4} \approx 11$ km EOSs considered.

Figure 3 also includes, as an approximate reference point, the mismatch from the simulations performed with two different resolutions, the higher of which matches the

effective resolutions of the $R_{1.4} \approx 11$ km and $R_{1.4} \approx 14$ km evolutions (see Appendix C for details). This reference mismatch confirms that the thermal differences are negligible for EOSs that differ only in the value of the M^* density-transition parameter, n_0, (shown in green). However, the mismatches in at least one of the spectral peaks are indeed numerically significant for all other pairs of EOSs considered.

We quantify the relative mismatch between the first and second spectral peaks for the $R_{1.4} \approx 14$ km EOSs in Fig. 4, calculated using the same method described above but with appropriately adjusted frequency ranges. Although the first spectral peaks have slightly larger mismatches for these stiffer EOSs, we find that the second peak still dominates the overall mismatch by a factor of $\mathcal{M}_2/\mathcal{M}_1 \sim 9$–16, for the models that vary in the thermal α parameters (blue crosses). In other words, the effect of varying the thermal treatment for the $R_{1.4} \approx 14$ km EOS is still primarily concentrated around the second spectral peak.

From these observations, we draw a few key conclusions. First, the peak frequency alone is insufficient to encapsulate the entirety of the differences between two spectra, even in the limit of very small changes to the underlying EOS. This is illustrated most directly by the $\Delta R_{1.4} = -54$ m case, for which the spectrum differs significantly from the baseline model, despite negligible differences in f_2. Figure 1 also shows that reducing $R_{1.4}$ by -120 m leads to a comparable shift in the peak frequency as increasing $R_{1.4}$ by $+116$ m, but the mismatch is significantly larger in the former case. These observations highlight the need to consider global mismatches, together with the peak frequency, to fully characterize the differences between two spectra, and suggests some limitations to how completely the quasiuniversal relations (which focus on a single peak frequency) can be used to characterize a spectrum.

Second, we find that varying the thermal treatment can lead to larger shifts in f_2 than varying the cold EOS by ± 120 m. Moreover, when considering the integrated (global) mismatch between spectra, we find that current uncertainties in the thermal physics lead to mismatches comparable to the mismatches that are found when the cold EOS is varied by -54 to $+116$ m. This implies that if the cold EOS is known at the level of $\pm \sim 120$ m in $R_{1.4}$—as will be possible within $\sim$1 year of binary neutron star inspiral observations with CE [39,40]—the postmerger GW spectra can be used to directly probe the finite-temperature part of the EOS.

C. Distinguishability of the postmerger GWs

We turn now to the question of how well these thermal signatures in the postmerger GWs can be measured, with current and upcoming detectors. To quantify this, we use the horizon distance, which defines the maximum distance at which two signals can be distinguished according to

$$d_{\rm hor} = \frac{d_i \rho_i}{\rho_{\rm distinguish}}, \tag{4}$$

where ρ_i is a reference signal-to-noise ratio (SNR) evaluated at a distance d_i. We assume that the SNRs of the individual spectra, ρ_i, are similar to one another for a given pair of EOSs, and thus use their average SNR as the reference when computing the horizon distances. Finally, $\rho_{\rm distinguish}$ represents the SNR required to distinguish between two GW spectra, which is given by

$$\rho_{\rm distinguish} = \max\left[\frac{e}{\sqrt{2\mathcal{M}}}, \rho_{\rm thresh}\right], \tag{5}$$

for distinguishability at 90% confidence level [60]. The threshold parameter, $\rho_{\rm thresh}$, imposes a minimum SNR requirement for detectability of the signal. We use a threshold for detectability of $\rho_{\rm thresh} = 5$.

We use our three-peak templates (shown in Figs. 1 and 2; see also Appendix C) to compute the horizon distances. We note that our integration bounds of $f = 2$–5.5 kHz (1.4–4 kHz) for the $R_{1.4} \approx 11$ km ($R_{1.4} \approx 14$ km) EOSs intentionally exclude the inspiral contributions to the spectra, in order to focus on the new information that can be gleaned postmerger. However, this choice also excludes lower-frequency differences that may emerge after the merger, such as from an $m = 1$ one-arm instability [61–63]. Thus, the mismatches and horizon distances reported in this work should be viewed as conservative lower limits, as a more sophisticated template that includes such features might expose additional differences.

Figure 5 shows the resulting horizon distances for which various pairs of EOSs could be distinguished. In the top panel, we show pairs of EOSs that vary in their thermal treatment with a soft cold EOS ($R_{1.4} \approx 11$ km), while in the bottom panel, we show the pairs of models that vary in their thermal treatment with a stiff cold EOS ($R_{1.4} \approx 14$ km). We compute horizon distances for two different detector noise curves: aLIGO shown in blue [57], and the 20 km configuration of Cosmic Explorer that has been tuned for postmerger sensitivity (CE-20 pm) in red [44].

With the design sensitivity of the current aLIGO instruments, we find that, even for the most extreme differences in thermal treatment, the resulting GW spectra would only be distinguishable for extremely nearby mergers (within 12 Mpc). Given that the closest neutron star merger every century is expected to be roughly 13^{+9}_{-4} Mpc away [64], it is not very likely that we will be able to directly measure these thermal effects with the current generation of detectors. However, with the sensitivity of CE-20 pm, the horizon distances increase significantly, to up to 83 Mpc and 208 Mpc for resolving thermal effects in the $R_{1.4} \approx 11$ km and $R_{1.4} \approx 14$ km cold EOSs, respectively.

It is interesting to observe that the thermal effects are more easily distinguishable for the $R_{1.4} \approx 14$ km EOSs,

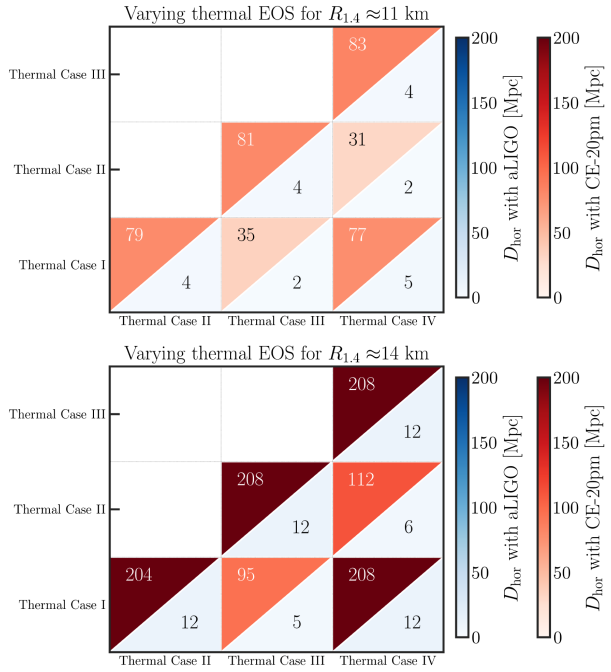

FIG. 5. Horizon distances (in Mpc) to which different pairs of EOS variations would be distinguishable at 90% confidence, assuming the design sensitivity of aLIGO (in blue) or the projected sensitivity of the CE-20 pm configuration (in red) and an SNR threshold for distinguishability of 5.

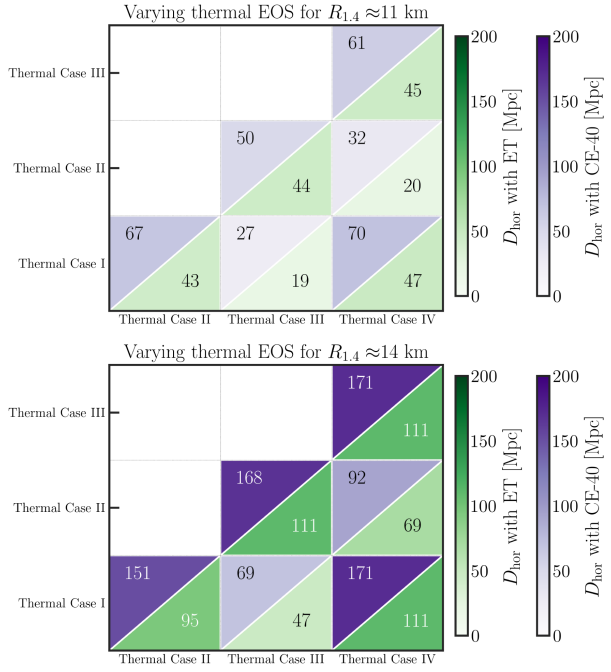

FIG. 6. Horizon distances (in Mpc) to which different pairs of EOS variations would be distinguishable at 90% confidence, assuming the projected sensitivity of Einstein Telescope (in green) or the 40 km configuration of Cosmic Explorer (in purple) and an SNR threshold for distinguishability of 5.

despite the fact that the mergers evolved with the $R_{1.4} \approx 11$ km cold EOS experience more heating and larger shifts in the peak frequencies (5% fractional variation in f_2 for the $R_{1.4} \approx 11$ km EOSs, compared to 2% shifts for the $R_{1.4} \approx 14$ km EOSs; see Table I). This is driven in part by the fact that the spectra peak at lower frequencies ($\sim$2.6 kHz) for the $R_{1.4} \approx 14$ km evolutions, where the detectors are significantly more sensitive. However, the difference in the central peak frequency does not entirely explain the larger mismatches.

We confirm this with a simple test that shifts the CE-20 pm noise curve down by 800 Hz, which is the approximate difference in peak frequencies between the $R_{1.4} \approx 11$ km and $R_{1.4} \approx 14$ km EOSs. This artificially ensures that the $R_{1.4} \approx 14$ km spectra peak at frequencies where the detector is comparably sensitive. Even in this case, we find that the horizon distances reach as far as $\sim$150 Mpc for the most disparate thermal treatments. This implies that the spectra are significantly more distinguishable than we find for the $R_{1.4} \approx 11$ km spectra, despite having smaller differences in f_2. This is due to slightly larger differences in the first and third spectral speaks for these EOSs, although the effect of changing the thermal treatment is still most concentrated in the second spectral peak (see Fig. 4).

We note that, even though the thermal effects led to comparable *global* mismatches compared to the changes in the cold EOS (see Fig. 3), the thermal differences will be slightly harder to distinguish, than would be estimated based on the "equivalent" change to $R_{1.4}$. As an example, for the baseline vs $\Delta R_{1.4} = +116$ m cold EOS comparison, the postmerger spectra could be distinguished at distances of up to 107 Mpc with the sensitivity of CE-20 pm. The (slightly) lower horizon distances for the $R_{1.4} \approx 11$ km EOSs with varied thermal prescriptions are a consequence of the frequencies at which the spectra differ: as was seen in Fig. 3, varying the cold EOS also produced significant differences in the first (lower-frequency) peak, while the variations in the thermal treatment lead to differences that are concentrated around the second peak. Although the second peak is louder, it is at higher frequencies, where the detectors are less sensitive. This poses an additional challenge for measuring thermal effects in the postmerger GWs; however, the horizon distances found here indicate that such constraints are nevertheless within reach for the next generation of detectors.

Finally, we also compute the horizon distances for the same pairs of EOSs, assuming the projected sensitivity of ET [15,65] and the 40 km configuration of Cosmic Explorer (CE-40) [14,66] in Fig. 6. For distinguishing the thermal effects, we find horizon distances of up to 70 Mpc (47 Mpc) for the $R_{1.4} \approx 11$ km EOSs and 171 Mpc (111 Mpc) for the $R_{1.4} \approx 14$ km EOSs, with CE-40 (ET). For both detectors, we find that at least some of the thermal prescriptions would be distinguishable for an event at the distance of GW170817. Thus, we conclude that the 20 km "postmerger" tuned configuration of CE gives the best

prospects for resolving thermal effects, but that the XG era is highly promising with any of these detectors.

IV. DISCUSSION AND CONCLUSIONS

In this work, we have shown that the uncertainties in the finite-temperature part of the EOS can alter the postmerger GWs by a degree comparable to changing the cold EOS by $\pm \sim 120$ m in radius (or, equivalently, by $\pm 5\%$ in the cold pressure at supranuclear densities). This suggests that it may be possible to derive new constraints on the physics of finite-temperature dense matter, if the cold EOS can be pinned down at this level. Recent estimates have suggested that observations of binary neutron star inspirals in the XG era will constrain the cold EOS to within 50–200 m in radius [39,40], implying that such constraints will indeed be within reach.

We find that the finite-temperature effects lead to spectral differences that are dominated by the second (dominant) peak, whereas varying the cold EOS toward smaller radii leads to more significant changes in the first peak as well. Because the detector sensitivity decreases rapidly with frequency, this makes the thermal effects slightly more challenging to detect. Nevertheless, we find horizon distances of up to 83 Mpc for distinguishing different thermal treatments for a soft cold EOS ($R_{1.4} \approx 11$ km) and up to 208 Mpc for a stiffer cold EOS ($R_{1.4} \approx 14$ km), when assuming the sensitivity of the 20 km postmerger tuned configuration of CE. The maximum horizon distances for distinguishing thermal effects given the 40 km configuration of CE or ET are ∼20–85% closer; but, in both cases, at least some of the thermal prescriptions would still be distinguishable for an event at the distance of GW170817. Building a framework to measure thermal parameters from a future GW signal requires additional parameter estimation studies, beyond the scope of this work. Nevertheless, these results indicate that the XG era is highly promising for distinguishing new finite-temperature effects from the postmerger GWs with any of these proposed detectors, with the CE-20 pm configuration offering the best prospects, and they provide new motivation for parameter estimation studies to further explore these detection prospects.

Finally, we note that the strength of the thermal effects is likely to also depend on the total mass and mass ratio of the system, and may be sensitive also to the treatment of neutrino transport [e.g., [35]]. Other effects such as nonzero initial spins [67], bulk viscosity arising after the merger [41,42], or the effects of including additional degrees of freedom [e.g., [68–74]] may also contribute to spectral distortions of similar magnitude to what have been studied here. In particular, some classes of phase transitions may not be constrained by the inspiral GWs alone, posing an additional challenge for pinning down the cold EOS at the level required for constraining these thermal models [75,76]. Finally, while our templates accurately capture the features of the three primary spectral peaks, they may miss out on additional differences between the spectra such as the emergence of spiral modes or one-arm instabilities. By construction, our smoothed templates also do not capture the finest-scale features of the spectra. As a result, the horizon distance estimates provided in this work should not be considered as the final word. Rather, these horizons provide a promising indication that differences in the thermal physics can be measurable with next-generation facilities, if the cold EOS is sufficiently well constrained, and motivate the construction of faithful postmerger GW templates, to fully characterize the possible interplay with these additional effects.

ACKNOWLEDGMENTS

C. R. is supported by a joint postdoctoral fellowship at the Princeton Gravity Initiative and the Institute for Advanced Study, with support from the John N. Bahcall Fellowship Fund and Schmidt Futures. This work was in part supported by NSF Grant No. PHY-2145421 to the University of Arizona. The simulations presented in this work were carried out with the Stampede2 cluster at the Texas Advanced Computing Center and the Expanse cluster at San Diego Supercomputer Center, under XSEDE allocation PHY190020. The simulations were also performed, in part, with the Princeton Research Computing resources at Princeton University, which is a consortium of groups led by the Princeton Institute for Computational Science and Engineering (PIC-SciE) and Office of Information Technology's Research Computing.

APPENDIX A: CONSTRUCTION OF THE COLD EQUATIONS OF STATE

In this Appendix, we describe the construction of the sequence of cold EOSs used in this work. For the baseline $R_{1.4} \approx 11$ km model and the $R_{1.4} \approx 14$ km models, we use a generalized piecewise-polytropic (PWP) parametrization of the wff2 [77] or H4 EOSs [78] at high densities, with a parametrized representation of SLy [79] for the crust. We follow the generalized PWP framework of [46] and parametrize the EOS via three segments, which are divided at the fiducial densities $\rho_1 = 10^{14.87}$ g/cm^3 and $\rho_2 = 10^{14.99}$ g/cm^3. The pressure along a given segment is given by

$$P(\rho) = K_i \rho^{\Gamma_i} + \Lambda_i, \qquad \rho_{i-1} < \rho \leq \rho_i, \tag{A1}$$

where the coefficient, K_i, is determined by requiring differentiability,

$$K_i = K_{i-1} \left(\frac{\Gamma_{i-1}}{\Gamma_i} \right) \rho_{i-1}^{\Gamma_{i-1} - \Gamma_i}, \tag{A2}$$

TABLE III. Model parameters for the generalized piecewise polytropic representations of the $R_{1.4} \approx 11$ km and $R_{1.4} \approx 14$ km EOSs. $R_{1.4}$ indicates the radius of a $1.4M_\odot$ neutron star predicted by each EOS. The parameter ρ_0 is the density at which the high-density parametrization intersects the crust EOS, which is taken to be a generalized piecewise polytropic representation of SLy. The remaining four columns provide the four free parameters used to characterize Eqs. (A2)–(A3). Table is repeated from [33] with permission.

$R_{1.4}$ [km]	ρ_0 [g/cm^3]	$\log_{10} K_1$	Γ_1	Γ_2	Γ_3
11.12	1.309×10^{14}	−35.443	3.316	4.122	3.200
13.99	2.931×10^{13}	−23.110	2.502	1.511	2.366

and the parameter Λ_i is imposed to ensure continuity, such that

$$\Lambda_i = \Lambda_{i-1} + \left(1 - \frac{\Gamma_{i-1}}{\Gamma_i}\right) K_{i-1} \rho_{i-1}^{\Gamma_{i-1}}. \tag{A3}$$

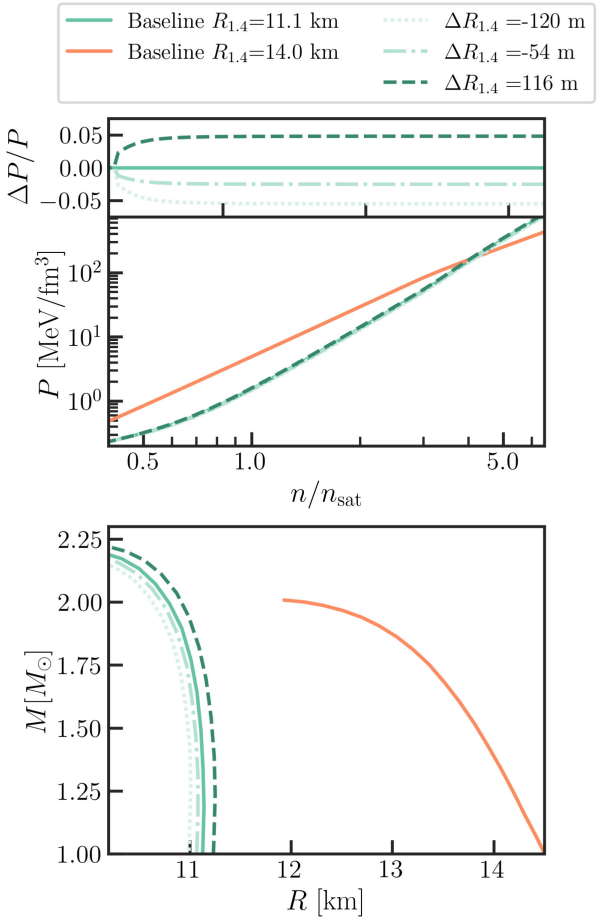

FIG. 7. Cold equations of state considered in this work. Top, inset: fractional difference in the zero-temperature pressure for the $R_{1.4} \approx 11$ km models, compared to the baseline model. Top, main figure: Pressure as a function of the density, relative to the nuclear saturation density $n_{\rm sat} = 0.16$ fm^{-3}. Bottom: corresponding mass-radius relations.

TABLE IV. Characteristic properties of the sequence of cold EOSs that deviate by a small degree from the $R_{1.4} \approx 11$ km baseline model. The first column indicates the labels used throughout this work. The second column lists the factor by which the pressure is scaled at all densities above $1.2\times$ the nuclear saturation density, compared to the baseline model. The final two columns report the characteristic radius and tidal deformability for a $1.4M_\odot$ neutron star.

EOS	P_c scale factor	$R_{1.4}$ [km]	$\Lambda_{1.4}$
$\Delta R_{1.4} = -120$ m	0.95	11.00	214
$\Delta R_{1.4} = -54$ m	0.975	11.07	223
Baseline	1.0	11.12	230
$\Delta R_{1.4} = +116$ m	1.05	11.24	244

There are thus four free parameters: K_1, Γ_1, Γ_2, Γ_3. From these parameters and the low-density EOS, all other K_i and Λ_i are uniquely determined. The fit procedure to construct the $R_{1.4} \approx 11$ km and $R_{1.4} \approx 14$ km EOSs has been described previously in Appendix A of [33], but we repeat the relevant model parameters in Table III for convenience.

To construct a sequence of new models that deviate by a small degree from the baseline $R_{1.4} \approx 11$ km EOS, we systematically scale the pressure above $\rho \geq 1.2\rho_{\rm sat}$ by a constant factor, ranging from 0.95 to 1.05. Between $\rho_{\rm sat}$ and $1.2\rho_{\rm sat}$, we linearly connect between this scaled pressure and the baseline model, which we use for all densities below $\rho_{\rm sat}$. The resulting EOSs are shown in Fig. 7, and their characteristic properties are summarized in Table IV.

In extending these cold EOSs to finite temperatures, we follow the framework of [45], with all details identical to the implementation in [33].

APPENDIX B: TEMPORAL EVOLUTION OF THE POSTMERGER GRAVITATIONAL WAVES

In this Appendix, we analyze the temporal evolution of the postmerger gravitational wave signals for our simulations. To that end, we compute spectrograms of the strain, $h(t)$, using time bins of length $350M_\odot$, with overlap of 75%. We show these spectrograms in Figs. 8–10.

The GW power for the $R_{1.4} \approx 11$ km models decays relatively quickly, within the first ∼10 ms postmerger. In contrast, the $R_{1.4} \approx 14$ km spectra are more temporally extended, with significant power still present at 10 ms after the merger. We also note the presence of a small drift in the peak frequencies for some models with the $R_{1.4} \approx 14$ km cold EOS (e.g., thermal prescription II; top right figure of Fig. 10). In order to capture these late-time features, we evolved the $R_{1.4} \approx 14$ km models to ∼20 ms after the merger, at which time the strain is approximately stationary and the power starts decaying.

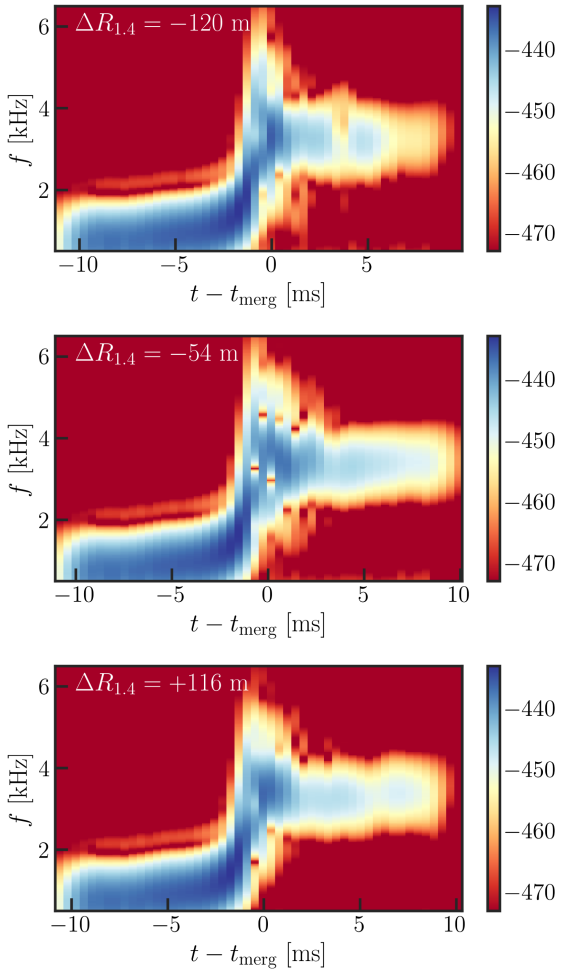

FIG. 8. Spectra for the $R_{1.4} \approx 11$ km cold EOSs. The strain includes the dominant $\ell = m = 2$ mode, and assumes a face-on orientation for a source directly overhead at a distance of 40 Mpc. The power is shown by the color, with decibel ($20\log_{10}$) scaling.

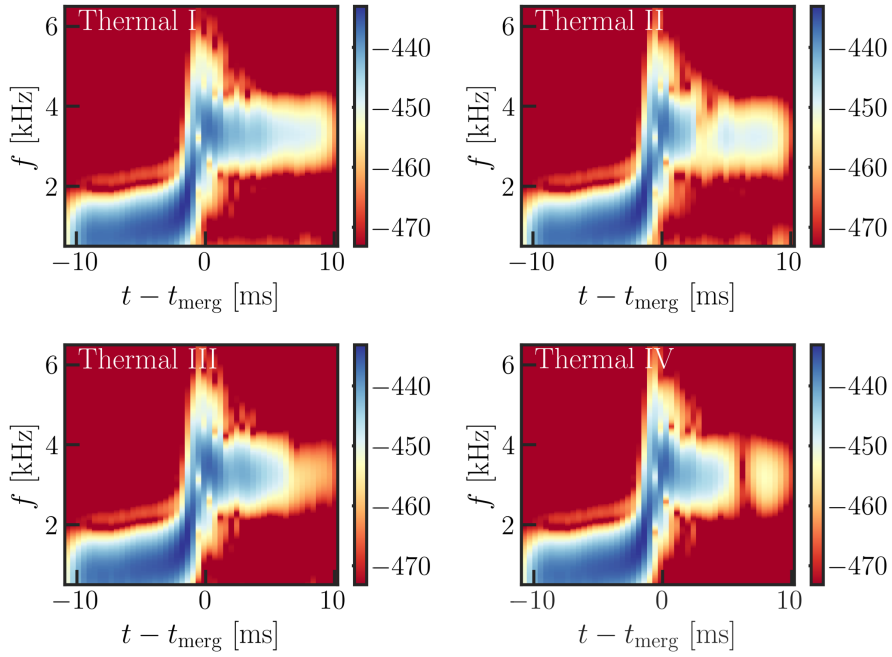

FIG. 9. Same as Fig. 8, but for the $R_{1.4} \approx 11$ km EOSs with different thermal treatments.

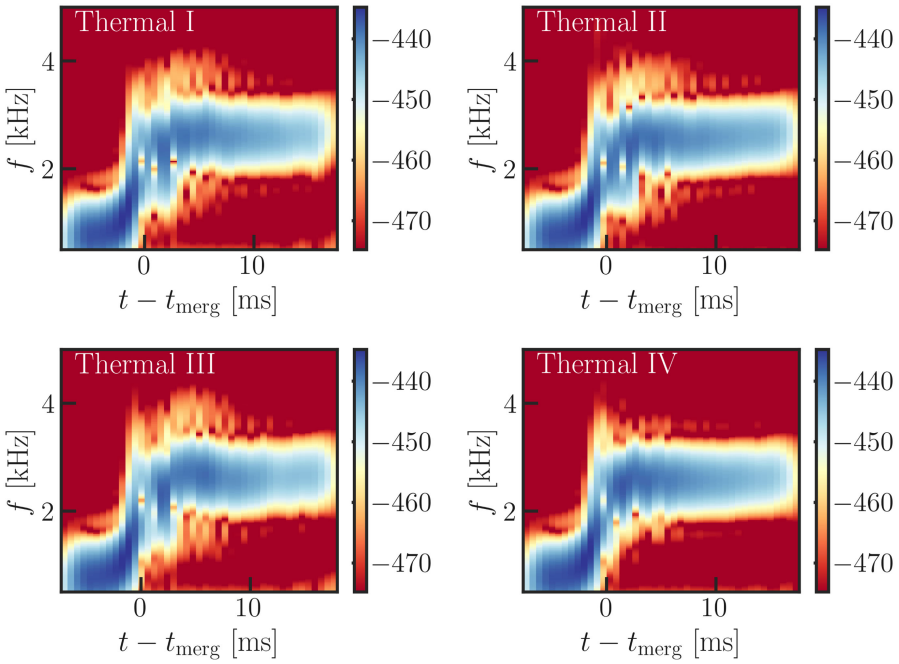

FIG. 10. Same as Fig. 8, but for the $R_{1.4} \approx 14$ km EOSs with different thermal treatments.

APPENDIX C: POSTMERGER GRAVITATIONAL WAVES AND TEMPLATE FITS

We extract the postmerger GWs from our simulations using the Newman-Penrose scalar, ψ_4, which is decomposed onto $s = -2$ spin-weighted spherical harmonics at large radii ($r = 300M_\odot$). We calculate the $+$ and $\times$ polarizations of the GW strain via the relation, $\psi_4 = \ddot{h}_+ - i\ddot{h}_\times$, using the fixed-frequency integration method of [80].

To compute the spectra shown in this work, we first apply a Tukey window with shape parameter of 0.25 to the time-series strain, and window the postmerger signal to have the same length, for all simulations within a given comparison (e.g., all $R_{1.4} \approx 11$ km models or all $R_{1.4} \approx 14$ km models). We then calculate the characteristic strain according to

$$h_c = 2f|\tilde{h}(f)|, \tag{C1}$$

where $\tilde{h}(f)$ is the Fourier transform of the strain, $h(t) = h_+ - ih_\times$. Finally, we apply a fourth-order Butterworth bandpass filter to the characteristic strain, in order to excise the inspiral contribution and any high-frequency noise. We apply the filter over a frequency range of 2–5.5 kHz for the $R_{1.4} \approx 11$ km EOSs and 1.4–4 kHz for the $R_{1.4} \approx 14$ km EOSs. These frequency bounds conservatively bracket the main postmerger signal, which we take to start just below the instantaneous GW frequency at merger and to end when the signal has dropped $\sim 100\times$ below the amplitude of the dominant spectral peak. In computing the spectra used in this work, we assume a face-on orientation and an optimal detector response, corresponding to a signal directly overhead. We show the resulting spectra, including the dominant $\ell = m = 2$ mode, as the thin lines in Fig. 11.

These spectra exhibit a high degree of noise on small-frequency scales, which we find leads to biases in the calculation of the mismatch integrals. Such high-frequency noise can be the result of either numerical error or stochasticity due to the highly turbulent state of the merger remnant following merger. In order to reduce the dependence of the mismatches on these small-scale features, which are not physically significant, for e.g., a signal-to-noise calculation, we fit the spectra with a simplified template model. A variety of phenomenological templates have been introduced previously, ranging from templates based on sine-Gaussian wavelets [e.g., [81,82]] to exponentially damped sinusoids [e.g., [13,83–86]]. Other approaches have constructed templates directly from numerical relativity data, e.g., using a reduced basis set derived from principal component analysis [12] or using a hierarchical model [87]. Recently, [88] introduced a "partially informed" template, which combines a wavelet basis set with relations calibrated to a large database of numerical relativity simulations.

In this work, our goal is to agnostically capture the three dominant spectral peaks present in our simulations. To that end, we adopt a model constructed from three Lorentzian profiles (similar to the approaches of [13,83–86]), and we additionally allow for nonzero skew to capture possible asymmetries in the peaks, which we find improves the quality of the fits. An individual profile is given by

$$\tilde{h}_i(f) = A_i\left[1 + \left(\frac{x}{1 + k_i \mathrm{sgn}[x]}\right)^2\right]^{-1}(1 - ix), \tag{C2}$$

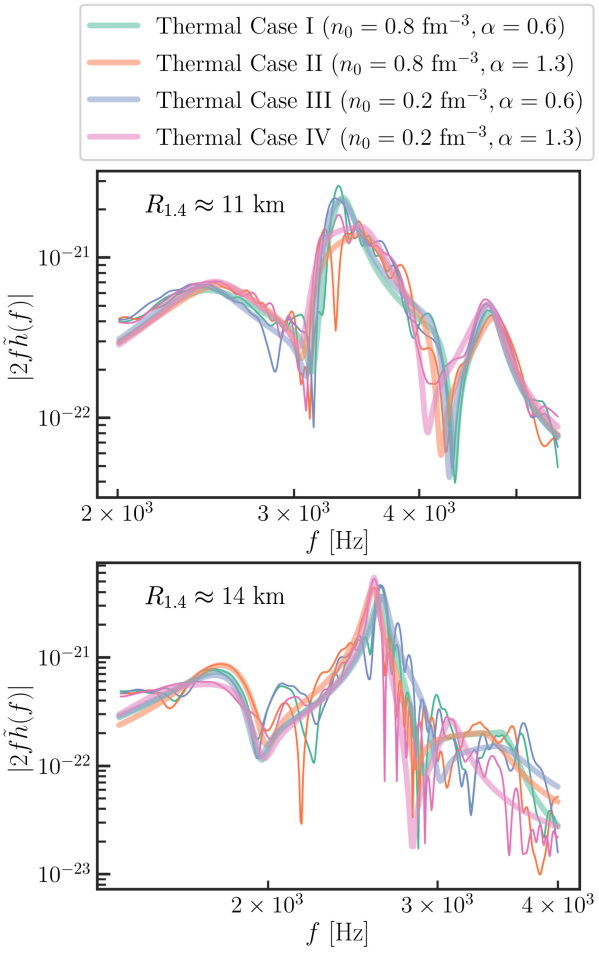

FIG. 11. Best-fit templates for the postmerger GW spectra. The $R_{1.4} \approx 11$ km EOSs with different thermal treatments are shown in the top panel, while the $R_{1.4} \approx 14$ km EOSs are shown in the bottom panel. Templates (in thick, smooth lines) are fit to the raw spectra (thin, darker lines) including the dominant $\ell = m = 2$ mode, assuming a face-on orientation with an optimal detector response factor and a source distance of 40 Mpc.

where A_i is the amplitude of the peak, k_i is a skew parameter that governs the peak asymmetry, the convenience parameter x is defined as

$$x = \frac{f - f_{\text{peak},i}}{Q_i}, \tag{C3}$$

and Q_i is related to the width of the peak.

We stitch together the individual peaks using a hyperbolic tangent smoothing, according to

$$\tilde{h}(f) = \tilde{h}_1(f) + \chi_1(1-\chi_2)[\tilde{h}_2(f) - \tilde{h}_1(f)] + \chi_2[\tilde{h}_3(f) - \tilde{h}_1(f)], \tag{C4}$$

where $\chi_{j=1,2}$ are the smoothing functions, which are given by

$$\chi_j = \frac{1 + \tanh[0.01(f - f_{\text{trans},j})]}{2}, \tag{C5}$$

and $f_{\text{trans},j}$ is the transition frequency that divides the adjacent spectral peaks.

In total, there are thus 11 parameters, including $A_i, Q_i, f_{\text{peak},i}$ for each of the three peaks and $f_{\text{trans,j}}$ for the two dividing frequencies. In order to simplify our fits, we fix the peak frequencies to the values obtained from Welch averages of our spectra. This procedure averages overlapping segments of the strain when computing the Fourier transform, and helps to more robustly identify the spectral peaks by reducing the noise. We note that the peak frequencies in Table I differ slightly from those reported in Paper I, due to differences in the Welch-averaging procedure. In Paper I, we required the $R_{1.4} \approx 11$ km and $R_{1.4} \approx 14$ km to have the same number of overlapping segments in the Welch averages, while in the present work, we require the length of the overlapping segments to be the same length (4 ms) for all simulations. The differences between these two conventions are small and do not affect the main results of either work.

After fixing the peak frequencies in this way, we are left with eight free parameters, which we fit to the (unaveraged) spectra. We perform a least-squares minimization to fit the magnitude of the characteristic strain. Although fitting the magnitude leaves the phase unconstrained, the template is used only to calculate overlaps, which are subsequently maximized with respect to the phase. We weight the fit by the projected noise curve for the CE-20 pm detector [44]. We show the resulting best-fit templates together with the original spectra, in Fig. 11.

Figure 12 shows the sensitivity of the postmerger spectra and corresponding templates to the resolution, for an EOS with intermediate stiffness ($R_{1.4} = 12$ km). This EOS also uses an intermediate set of M^* parameters ($n_0 = 0.12$ fm$^{-3}, \alpha = 0.8$), making it a convenient

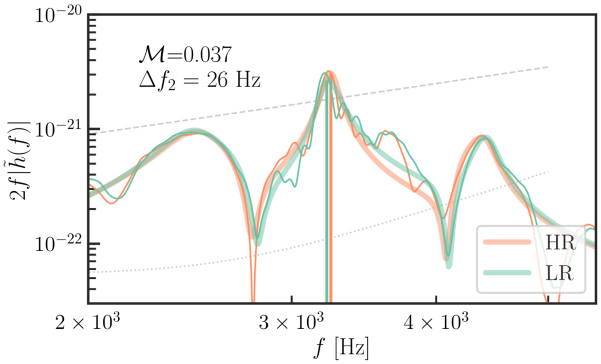

FIG. 12. Postmerger GW spectra (thin lines) and best-fit templates (thick lines) for two different resolutions. The low resolution ($dx = 195$ m) evolution is shown in teal, while a higher resolution ($dx = 156.25$ m) evolution is shown in orange. The EOS corresponds to an intermediate stiffness with $R_{1.4} = 12$ km [52].

TABLE V. Coefficient of determination, R^2, between the best-fit spectral templates and the (unaveraged) characteristic strain from our simulations.

Cold EOS	Variation to Cold EOS	Thermal case	R^2
$R_{1.4} \approx 11$ km	$\Delta R_{1.4} = -120$ m	I	0.85
	$\Delta R_{1.4} = -54$ m	I	0.88
	$\Delta R_{1.4} = +116$ m	I	0.89
$R_{1.4} \approx 11$ km	–	I	0.91
		II	0.88
		III	0.94
		IV	0.95
$R_{1.4} \approx 14$ km	–	I	0.91
		II	0.96
		III	0.86
		IV	0.96

(albeit approximate) reference point for the simulations explored in this work. The two resolutions correspond to a grid spacing on the innermost refinement level of $dx = 195$ m and $dx = 156.25$ m; or, equivalently, to placing ~100 or 125 points across the coordinate diameter of the initial neutron stars. The effective resolution of the high-resolution evolution is thus comparable to the resolutions used in the present work (i.e., covering the coordinate diameter of the initial neutron stars by ~125 grid points; see Sec. II B). For further details on this EOS and the evolutions from which these spectra were extracted, see [52]. We find negligible changes to the spectra as the resolution is increased by a factor of 1.25. In particular, we find that the dominant peak frequencies differ by only 26 Hz and that the mismatch between the best-fit spectra for the two resolutions is small as well, with $\mathcal{M} = 0.037$.

We report the coefficients of determination for the template fits in Table V. Given that our fits provide signals that have approximately the same SNR as the raw signals they are based on, we compute the R^2 statistic as a measure of goodness of fit. We find that the best-fit templates account for 84%–97% of the variation in the underlying spectra. To put this number in context, we also calculate the R^2 statistic between the two different resolutions, using the complete spectrum (i.e., not the template) from the low resolution simulation as an approximant of the high-resolution spectrum. We find that the low-resolution spectrum accounts for 89% of the variation found in the high-resolution spectrum, which is a comparable R^2 value to what we obtain for our template fits. In other words, the $\lesssim$15% "loss" we incur by using the templates in lieu of the complete spectra is comparable to the losses obtained by using a standard, instead of high, resolution in our evolutions.

We note that using the templates leads to mismatches that are always smaller than would be estimated from the raw spectra, because the templates effectively smooth out the smallest-scale differences. We report the mismatches calculated with both the raw spectra and our best-fit templates, for all combinations of models, in Table VI.

TABLE VI. Summary of mismatches calculated using either the raw spectra (in column 4) or the best-fit templates (in column 5), for various model comparisons. The final column reports the ratio of $\mathcal{M}$ calculated with the templates compared to the raw spectra. The first section reports mismatches for models that share the same cold $R_{1.4} \approx 11$ km EOS, while the second section reports mismatches for models with the same cold $R_{1.4} \approx 14$ km EOS. The third section reports the mismatches for models with the same thermal treatment (Case I), but that vary in their cold EOS. All mismatches use overlaps that have been maximized with respect to time and phase. Mismatches calculated using the smoothed spectral templates are typically smaller than those calculated from the raw spectra.

Shared EOS	Model A	Model B	$\mathcal{M}_{\rm raw}$	$\mathcal{M}_{\rm template}$	$\mathcal{M}_{\rm template}/\mathcal{M}_{\rm raw}$
$R_{1.4} \approx 11$ km	Thermal I	Thermal II	0.18	0.08	0.44
	Thermal I	Thermal III	0.06	0.02	0.25
	Thermal I	Thermal IV	0.09	0.08	0.81
	Thermal II	Thermal III	0.15	0.08	0.58
	Thermal II	Thermal IV	0.06	0.01	0.20
	Thermal III	Thermal IV	0.07	0.09	1.3
$R_{1.4} \approx 14$ km	Thermal I	Thermal II	0.48	0.14	0.30
	Thermal I	Thermal III	0.08	0.03	0.40
	Thermal I	Thermal IV	0.36	0.19	0.51
	Thermal II	Thermal III	0.60	0.20	0.34
	Thermal II	Thermal IV	0.12	0.04	0.36
	Thermal III	Thermal IV	0.51	0.26	0.50
Thermal I	$\Delta R_{1.4} = -120$ m	$\Delta R_{1.4} = -54$ m	0.40	0.14	0.33
	$\Delta R_{1.4} = -120$ m	Baseline [$R_{1.4} = 11.1$ km]	0.23	0.19	0.81
	$\Delta R_{1.4} = -120$ m	$\Delta R_{1.4} = +116$ m	0.21	0.16	0.74
	$\Delta R_{1.4} = -54$ m	Baseline [$R_{1.4} = 11.1$ km]	0.30	0.07	0.24
	$\Delta R_{1.4} = -54$ m	$\Delta R_{1.4} = +116$ m	0.30	0.09	0.31
	Baseline [$R_{1.4} = 11.1$ km]	$\Delta R_{1.4} = +116$ m	0.09	0.07	0.82

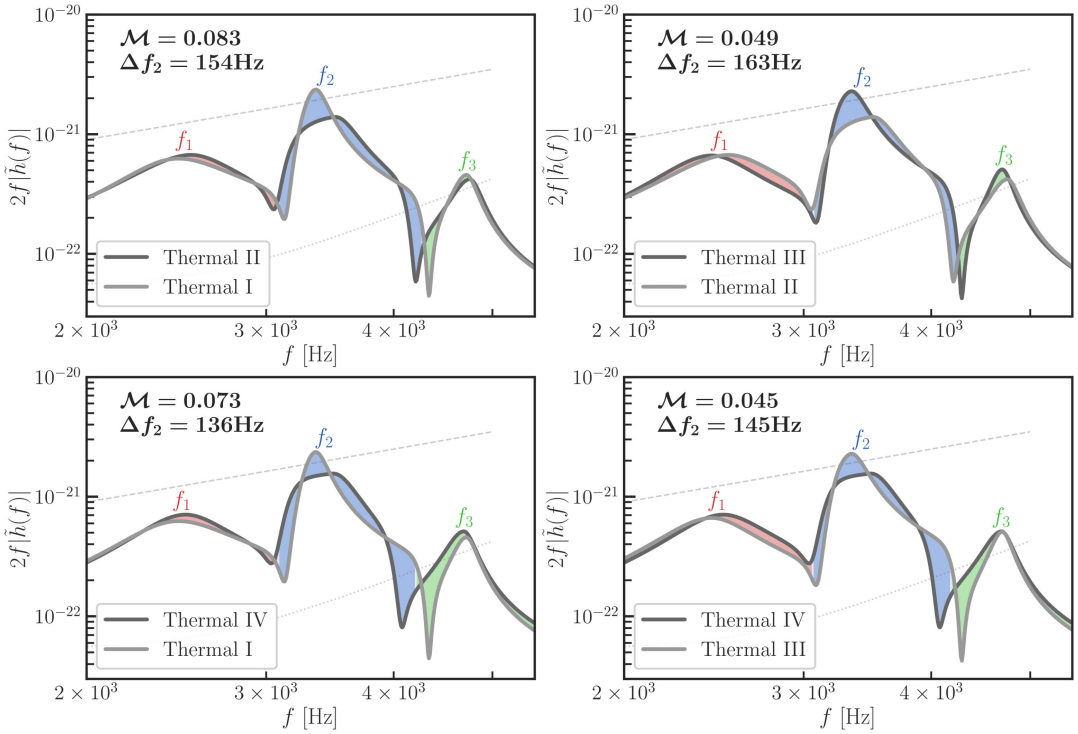

FIG. 13. Postmerger spectral templates for the $R_{1.4} \approx 11$ km EOSs that vary in their thermal treatment. The color coding is included to help visually distinguish the three spectral peaks (labeled f_1, f_2, and f_3) and to highlight the frequency dependence of the mismatches between each pair of spectra. The global mismatch (calculated over the entire frequency range shown) and the difference in peak frequency are included in the top corner, for reference. All other details are identical to Fig. 1.

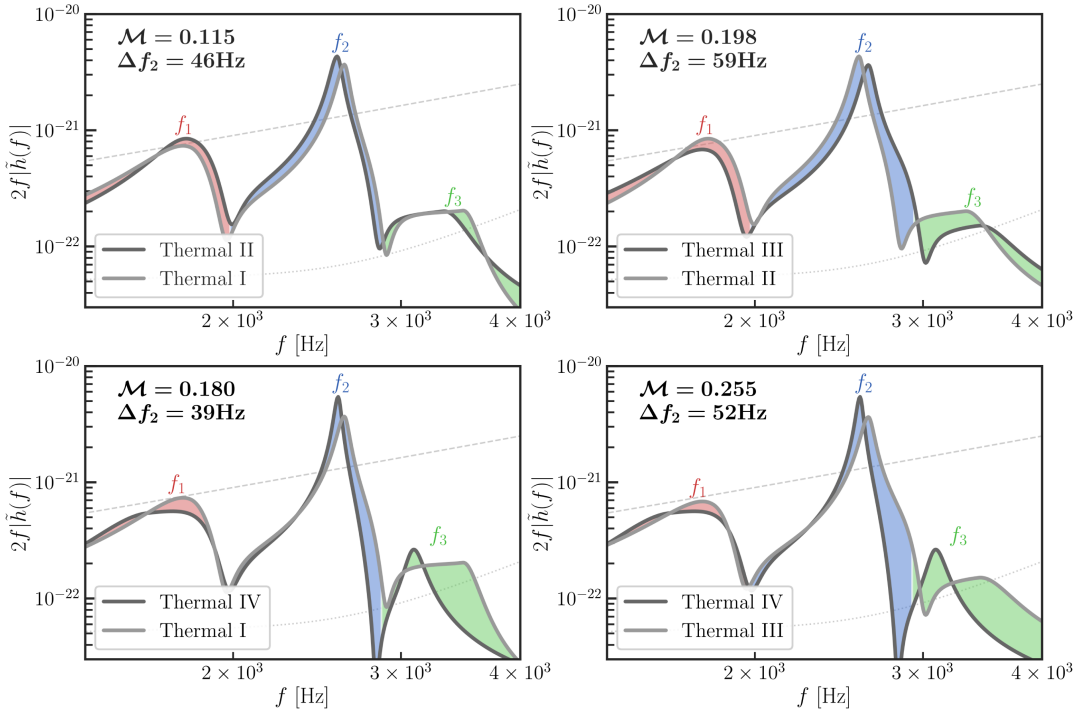

FIG. 14. Same as Fig. 13, but for the $R_{1.4} \approx 14$ km EOSs.

In all cases except one, the mismatches calculated with the templates are smaller than mismatches calculated with the raw spectra. For the one exception to this statement (the $R_{1.4} \approx 11$ km model with Thermal Case III vs IV), the mismatches are similar with the two calculation methods. The smaller mismatches require closer source distances for the models to be distinguished [Eq. (4)]. In other words, using the smoothed spectral templates makes it harder to distinguish between the various models. For these reasons, we use the templates when estimating the distinguishability (and, e.g., calculating horizon distances) in order to be as conservative as possible.

Finally, for completeness, Figs. 13 and 14 show the best-fit spectral templates for additional examples of the $R_{1.4} \approx 11$ km and $R_{1.4} \approx 14$ km EOSs with varying thermal prescriptions. These comparisons correspond to thermal models that differ in their α power-law parameter (see Table 1), which determines the rate at which the effective mass function decays with density, and which was found in Paper I to govern the location of the peak frequency of the postmerger spectra.

[1] L. Baiotti and L. Rezzolla, Binary neutron star mergers: A review of Einstein's richest laboratory, Rep. Prog. Phys. **80**, 096901 (2017).

[2] V. Paschalidis and N. Stergioulas, Rotating stars in relativity, Living Rev. Relativity **20**, 7 (2017).

[3] S. Bernuzzi, Neutron star merger remnants, Gen. Relativ. Gravit. **52**, 108 (2020).

[4] T. Dietrich, T. Hinderer, and A. Samajdar, Interpreting binary neutron star mergers: Describing the binary neutron star dynamics, modelling gravitational waveforms, and analyzing detections, Gen. Relativ. Gravit. **53**, 27 (2021).

[5] D. Radice, S. Bernuzzi, and A. Perego, The dynamics of binary neutron star mergers and GW170817, Annu. Rev. Nucl. Part. Sci. **70**, 95 (2020).

[6] A. Bauswein, H. T. Janka, K. Hebeler, and A. Schwenk, Equation-of-state dependence of the gravitational-wave signal from the ring-down phase of neutron-star mergers, Phys. Rev. D **86**, 063001 (2012).

[7] A. Bauswein and H. T. Janka, Measuring neutron-star properties via gravitational waves from binary mergers, Phys. Rev. Lett. **108**, 011101 (2012).

[8] K. Takami, L. Rezzolla, and L. Baiotti, Constraining the equation of state of neutron stars from binary mergers, Phys. Rev. Lett. **113**, 091104 (2014).

[9] S. Bernuzzi, T. Dietrich, and A. Nagar, Modeling the complete gravitational wave spectrum of neutron star mergers, Phys. Rev. Lett. **115**, 091101 (2015).

[10] M. Breschi, S. Bernuzzi, D. Godzieba, A. Perego, and D. Radice, Constraints on the maximum densities of neutron stars from postmerger gravitational waves with third-generation observations, Phys. Rev. Lett. **128**, 161102 (2022).

[11] C. A. Raithel and E. R. Most, Characterizing the breakdown of quasi-universality in postmerger gravitational waves from binary neutron star mergers, Astrophys. J. Lett. **933**, L39 (2022).

[12] J. A. Clark, A. Bauswein, N. Stergioulas, and D. Shoemaker, Observing gravitational waves from the post-merger phase of binary neutron star coalescence, Classical Quantum Gravity **33**, 085003 (2016).

[13] H. Yang, V. Paschalidis, K. Yagi, L. Lehner, F. Pretorius, and N. Yunes, Gravitational wave spectroscopy of binary neutron star merger remnants with mode stacking, Phys. Rev. D **97**, 024049 (2018).

[14] D. Reitze *et al.*, Cosmic explorer: The U.S. contribution to gravitational-wave astronomy beyond LIGO, Bull. Am. Astron. Soc. **51**, 035 (2019).

[15] M. Punturo *et al.*, The Einstein telescope: A third-generation gravitational wave observatory, Classical Quantum Gravity **27**, 194002 (2010).

[16] K. Ackley *et al.*, Neutron star extreme matter observatory: A kilohertz-band gravitational-wave detector in the global network, Pub. Astron. Soc. Aust. **37**, e047 (2020).

[17] A. Torres-Rivas, K. Chatziioannou, A. Bauswein, and J. A. Clark, Observing the post-merger signal of GW170817-like events with improved gravitational-wave detectors, Phys. Rev. D **99**, 044014 (2019).

[18] M. Evans *et al.*, Cosmic explorer: A submission to the NSF MPSAC ngGW subcommittee, arXiv:2306.13745.

[19] B. P. Abbott *et al.* (LIGO Scientific and Virgo Collaborations), GW170817: Measurements of neutron star radii and equation of state, Phys. Rev. Lett. **121**, 161101 (2018).

[20] L. Baiotti, Gravitational waves from neutron star mergers and their relation to the nuclear equation of state, Prog. Part. Nucl. Phys. **109**, 103714 (2019).

[21] A. Guerra Chaves and T. Hinderer, Probing the equation of state of neutron star matter with gravitational waves from binary inspirals in light of GW170817: A brief review, J. Phys. G **46**, 123002 (2019).

[22] C. A. Raithel, Constraints on the neutron star equation of state from GW170817, Eur. Phys. J. A **55**, 80 (2019).

[23] K. Chatziioannou, Neutron star tidal deformability and equation of state constraints, Gen. Relativ. Gravit. **52**, 109 (2020).

[24] E. Annala, T. Gorda, E. Katerini, A. Kurkela, J. Nättilä, V. Paschalidis, and A. Vuorinen, Multimessenger constraints for ultradense matter, Phys. Rev. X **12**, 011058 (2022).

[25] R. Oechslin, H. T. Janka, and A. Marek, Relativistic neutron star merger simulations with non-zero temperature equations of state. 1. Variation of binary parameters and equation of state, Astron. Astrophys. **467**, 395 (2007).

[26] A. Bauswein, H. T. Janka, and R. Oechslin, Testing approximations of thermal effects in neutron star merger simulations, Phys. Rev. D **82**, 084043 (2010).

[27] Y. Sekiguchi, K. Kiuchi, K. Kyutoku, and M. Shibata, Gravitational waves and neutrino emission from the merger of binary neutron stars, Phys. Rev. Lett. **107**, 051102 (2011).
[28] F. Foucart, R. Haas, M. D. Duez, E. O'Connor, C. D. Ott, L. Roberts, L. E. Kidder, J. Lippuner, H. P. Pfeiffer, and M. A. Scheel, Low mass binary neutron star mergers: Gravitational waves and neutrino emission, Phys. Rev. D **93**, 044019 (2016).
[29] C. Palenzuela, S. L. Liebling, D. Neilsen, L. Lehner, O. L. Caballero, E. O'Connor, and M. Anderson, Effects of the microphysical equation of state in the mergers of magnetized neutron stars with neutrino cooling, Phys. Rev. D **92**, 044045 (2015).
[30] W. Kastaun, R. Ciolfi, and B. Giacomazzo, Structure of stable binary neutron star merger remnants: A case study, Phys. Rev. D **94**, 044060 (2016).
[31] D. Radice, General-relativistic large-eddy simulations of binary neutron star mergers, Astrophys. J. Lett. **838**, L2 (2017).
[32] C. Raithel, V. Paschalidis, and F. Özel, Realistic finite-temperature effects in neutron star merger simulations, Phys. Rev. D **104**, 063016 (2021).
[33] C. A. Raithel and V. Paschalidis, Influence of stellar compactness on finite-temperature effects in neutron star merger simulations, Phys. Rev. D **108**, 083029 (2023).
[34] A. Figura, J. J. Lu, G. F. Burgio, Z. H. Li, and H. J. Schulze, Hybrid equation of state approach in binary neutron-star merger simulations, Phys. Rev. D **102**, 043006 (2020).
[35] J. Fields, A. Prakash, M. Breschi, D. Radice, S. Bernuzzi, and A. da Silva Schneider, Thermal effects in binary neutron star mergers, Astrophys. J. Lett. **952**, L36 (2023).
[36] V. Villa-Ortega, A. Lorenzo-Medina, J. Calderón Bustillo, M. Ruiz, D. Guerra, P. Cerdá-Duran, and J. A. Font, Self-consistent treatment of thermal effects in neutron-star post-mergers: Observational implications for third-generation gravitational-wave detectors, arXiv:2310.20378.
[37] M. Miravet-Tenés, D. Guerra, M. Ruiz, P. Cerdá-Durán, and J. A. Font, Identifying thermal effects in neutron star merger remnants with model-agnostic waveform reconstructions and third-generation detectors, arXiv:2401.02493.
[38] Z. Carson, K. Chatziioannou, C.-J. Haster, K. Yagi, and N. Yunes, Equation-of-state insensitive relations after GW170817, Phys. Rev. D **99**, 083016 (2019).
[39] K. Chatziioannou, Uncertainty limits on neutron star radius measurements with gravitational waves, Phys. Rev. D **105**, 084021 (2022).
[40] D. Finstad, L. V. White, and D. A. Brown, Prospects for a precise equation of state measurement from Advanced LIGO and cosmic explorer, Astrophys. J. **955**, 45 (2023).
[41] P. Hammond, I. Hawke, and N. Andersson, Impact of nuclear reactions on gravitational waves from neutron star mergers, Phys. Rev. D **107**, 043023 (2023).
[42] E. R. Most, A. Haber, S. P. Harris, Z. Zhang, M. G. Alford, and J. Noronha, Emergence of microphysical viscosity in binary neutron star post-merger dynamics, Astrophys. J. Lett. **967**, L14 (2024).
[43] P. L. Espino, P. Hammond, D. Radice, S. Bernuzzi, R. Gamba, F. Zappa, L. F. L. Micchi, and A. Perego, Neutrino trapping and out-of-equilibrium effects in binary neutron star merger remnants, Phys. Rev. Lett. **132**, 211001 (2024).
[44] V. Srivastava, D. Davis, K. Kuns, P. Landry, S. Ballmer, M. Evans, E. D. Hall, J. Read, and B. S. Sathyaprakash, Science-driven tunable design of cosmic explorer detectors, Astrophys. J. **931**, 22 (2022).
[45] C. A. Raithel, F. Ozel, and D. Psaltis, Finite-temperature extension for cold neutron star equations of state, Astrophys. J. **875**, 12 (2019).
[46] M. F. O'Boyle, C. Markakis, N. Stergioulas, and J. S. Read, Parametrized equation of state for neutron star matter with continuous sound speed, Phys. Rev. D **102**, 083027 (2020).
[47] C. A. Raithel, P. Espino, and V. Paschalidis, Finite-temperature effects in dynamical spacetime binary neutron star merger simulations: Validation of the parametric approach, Mon. Not. R. Astron. Soc. **516**, 4792 (2022).
[48] M. D. Duez, Y. T. Liu, S. L. Shapiro, and B. C. Stephens, Excitation of MHD modes with gravitational waves: A testbed for numerical codes, Phys. Rev. D **72**, 024029 (2005).
[49] V. Paschalidis, Z. Etienne, Y. T. Liu, and S. L. Shapiro, Head-on collisions of binary white dwarf–neutron stars: Simulations in full general relativity, Phys. Rev. D **83**, 064002 (2011).
[50] Z. B. Etienne, V. Paschalidis, Y. T. Liu, and S. L. Shapiro, Relativistic MHD in dynamical spacetimes: Improved EM gauge condition for AMR grids, Phys. Rev. D **85**, 024013 (2012).
[51] Z. B. Etienne, V. Paschalidis, R. Haas, P. Mösta, and S. L. Shapiro, IllinoisGRMHD: An open-source, user-friendly GRMHD code for dynamical spacetimes, Classical Quantum Gravity **32**, 175009 (2015).
[52] C. A. Raithel and V. Paschalidis, Improving the convergence order of binary neutron star merger simulations in the Baumgarte- Shapiro-Shibata-Nakamura formulation, Phys. Rev. D **106**, 023015 (2022).
[53] E. Gourgoulhon, P. Grandclement, J.-A. Marck, J. Novak, and K. Taniguchi, Lorene, https://lorene.obspm.fr/.
[54] N. Stergioulas, A. Bauswein, K. Zagkouris, and H.-T. Janka, Gravitational waves and nonaxisymmetric oscillation modes in mergers of compact object binaries, Mon. Not. R. Astron. Soc. **418**, 427 (2011).
[55] L. Rezzolla and K. Takami, Gravitational-wave signal from binary neutron stars: A systematic analysis of the spectral properties, Phys. Rev. D **93**, 124051 (2016).
[56] A. Bauswein and N. Stergioulas, Spectral classification of gravitational-wave emission and equation of state constraints in binary neutron star mergers, J. Phys. G **46**, 113002 (2019).
[57] aLIGO design sensitivity, https://dcc.ligo.org/public/0149/T1800044/005/aLIGODesign.txt, accessed: 2023-04-03.
[58] L. Lindblom, B. J. Owen, and D. A. Brown, Model waveform accuracy standards for gravitational wave data analysis, Phys. Rev. D **78**, 124020 (2008).
[59] S. T. McWilliams, B. J. Kelly, and J. G. Baker, Observing mergers of non-spinning black-hole binaries, Phys. Rev. D **82**, 024014 (2010).
[60] E. Baird, S. Fairhurst, M. Hannam, and P. Murphy, Degeneracy between mass and spin in black-hole-binary waveforms, Phys. Rev. D **87**, 024035 (2013).
[61] W. E. East, V. Paschalidis, F. Pretorius, and S. L. Shapiro, Relativistic simulations of eccentric binary neutron star

mergers: One-arm spiral instability and effects of neutron star spin, Phys. Rev. D **93**, 024011 (2016).
[62] V. Paschalidis, W. E. East, F. Pretorius, and S. L. Shapiro, One-arm spiral instability in hypermassive neutron stars formed by dynamical-capture binary neutron star mergers, Phys. Rev. D **92**, 121502 (2015).
[63] D. Radice, S. Bernuzzi, and C. D. Ott, One-armed spiral instability in neutron star mergers and its detectability in gravitational waves, Phys. Rev. D **94**, 064011 (2016).
[64] E. Burns, Neutron star mergers and how to study them, Living Rev. Relativity **23**, 4 (2020).
[65] Einstein telescope sensitivity curves, https://apps.et-gw.eu/tds/?content=3&r=14065, accessed: 2023-04-03.
[66] Cosmic explorer sensitivity curves, https://dcc.ligo.org/LIGO-P1600143/public, accessed: 2023-04-03.
[67] W. E. East, V. Paschalidis, F. Pretorius, and A. Tsokaros, Binary neutron star mergers: Effects of spin and post-merger dynamics, Phys. Rev. D **100**, 124042 (2019).
[68] Y. Sekiguchi, K. Kiuchi, K. Kyutoku, and M. Shibata, Effects of hyperons in binary neutron star mergers, Phys. Rev. Lett. **107**, 211101 (2011).
[69] D. Radice, S. Bernuzzi, W. Del Pozzo, L. F. Roberts, and C. D. Ott, Probing extreme-density matter with gravitational wave observations of binary neutron star merger remnants, Astrophys. J. Lett. **842**, L10 (2017).
[70] A. Bauswein, N.-U. F. Bastian, D. B. Blaschke, K. Chatziioannou, J. A. Clark, T. Fischer, and M. Oertel, Identifying a first-order phase transition in neutron star mergers through gravitational waves, Phys. Rev. Lett. **122**, 061102 (2019).
[71] E. R. Most, L. Jens Papenfort, V. Dexheimer, M. Hanauske, H. Stoecker, and L. Rezzolla, On the deconfinement phase transition in neutron-star mergers, Eur. Phys. J. A **56**, 59 (2020).
[72] S. Blacker, H. Kochankovski, A. Bauswein, A. Ramos, and L. Tolos, Thermal behavior as indicator for hyperons in binary neutron star merger remnants, Phys. Rev. D **109**, 043015 (2024).
[73] P. L. Espino, A. Prakash, D. Radice, and D. Logoteta, Revealing phase transition in dense matter with gravitational wave spectroscopy of binary neutron star mergers, Phys. Rev. D **109**, 123009 (2024).
[74] V. Vijayan, N. Rahman, A. Bauswein, G. Martínez-Pinedo, and I. L. Arbina, Impact of pions on binary neutron star mergers, Phys. Rev. D **108**, 023020 (2023).
[75] C. A. Raithel and E. R. Most, Degeneracy in the inference of phase transitions in the neutron star equation of state from gravitational wave data, Phys. Rev. Lett. **130**, 201403 (2023).
[76] C. A. Raithel and E. R. Most, Tidal deformability doppelgänger: Implications of a low-density phase transition in the neutron star equation of state, Phys. Rev. D **108**, 023010 (2023).
[77] R. B. Wiringa, V. Fiks, and A. Fabrocini, Equation of state for dense nucleon matter, Phys. Rev. C **38**, 1010 (1988).
[78] B. D. Lackey, M. Nayyar, and B. J. Owen, Observational constraints on hyperons in neutron stars, Phys. Rev. D **73**, 024021 (2006).
[79] F. Douchin and P. Haensel, A unified equation of state of dense matter and neutron star structure, Astron. Astrophys. **380**, 151 (2001).
[80] C. Reisswig and D. Pollney, Notes on the integration of numerical relativity waveforms, Classical Quantum Gravity **28**, 195015 (2011).
[81] K. Chatziioannou, J. A. Clark, A. Bauswein, M. Millhouse, T. B. Littenberg, and N. Cornish, Inferring the post-merger gravitational wave emission from binary neutron star coalescences, Phys. Rev. D **96**, 124035 (2017).
[82] M. Wijngaarden, K. Chatziioannou, A. Bauswein, J. A. Clark, and N. J. Cornish, Probing neutron stars with the full premerger and postmerger gravitational wave signal from binary coalescences, Phys. Rev. D **105**, 104019 (2022).
[83] K. Hotokezaka, K. Kiuchi, K. Kyutoku, T. Muranushi, Y.-i. Sekiguchi, M. Shibata, and K. Taniguchi, Remnant massive neutron stars of binary neutron star mergers: Evolution process and gravitational waveform, Phys. Rev. D **88**, 044026 (2013).
[84] A. Bauswein, N. Stergioulas, and H.-T. Janka, Exploring properties of high-density matter through remnants of neutron-star mergers, Eur. Phys. J. A **52**, 56 (2016).
[85] K. W. Tsang, T. Dietrich, and C. Van Den Broeck, Modeling the postmerger gravitational wave signal and extracting binary properties from future binary neutron star detections, Phys. Rev. D **100**, 044047 (2019).
[86] T. Soultanis, A. Bauswein, and N. Stergioulas, Analytic models of the spectral properties of gravitational waves from neutron star merger remnants, Phys. Rev. D **105**, 043020 (2022).
[87] P. J. Easter, P. D. Lasky, A. R. Casey, L. Rezzolla, and K. Takami, Computing fast and reliable gravitational waveforms of binary neutron star merger remnants, Phys. Rev. D **100**, 043005 (2019).
[88] M. Breschi, S. Bernuzzi, K. Chakravarti, A. Camilletti, A. Prakash, and A. Perego, Kilohertz gravitational waves from binary neutron star mergers: Numerical-relativity informed postmerger model, Phys. Rev. D **109**, 064009 (2024).